#### PATTERNS & PHENOTYPES



# Alleles of unc-33/CRMP exhibit defects during Caenorhabditis elegans epidermal morphogenesis

Rachel Prins | Peter Windsor | Bill R. Miller III | Stephanie Maiden |

<sup>1</sup>Department of Biology, Truman State University, Kirksville, Missouri, USA <sup>2</sup>Department of Chemistry, Truman State University, Kirksville, Missouri, USA

#### Correspondence

Stephanie Maiden, Department of Biology, Truman State University, 100 E. Normal Avenue, Kirksville, MO 63501, USA.

Email: smaiden@truman.edu

#### **Funding information**

National Science Foundation, Grant/ Award Numbers: CHE-1229354, CHE-1626238; Interdisciplinary Research Community Grant (IRCG) from the Office of Student Research at Truman State University

#### Abstract

**Background:** Microtubule-associated proteins regulate the dynamics, organization, and function of microtubules, impacting a number of vital cellular processes. CRMPs have been shown to control microtubule assembly and axon outgrowth during neuronal differentiation. While many microtubule-associated proteins have been linked to roles in cell division and neuronal development, it is still unclear the complement that control the formation of parallel microtubule arrays in epithelial cells.

**Results:** Here we show through time-lapse DIC microscopy that *Caenorhabditis elegans* embryos homozygous for the weak loss-of-function allele *unc-33(e204)* progress more slowly through epidermal morphogenesis, while animals homozygous for strong loss-of-function alleles exhibit more embryonic lethality. Identification of two novel missense mutations in *unc-33 (e572)*, Val476Gly, and Ser731Thr, lead to computational approaches to determine the potential effects of these changes on UNC-33/CRMP structure. Molecular dynamics simulations show that for Asp389Asn and Arg502His, two other known missense mutations, local changes in protein-protein hydrogen bonding affect the stability of the protein. However, the Val476Gly/Ser731Thr combination does not alter the structure or energetics of UNC-33 drastically when compared to the wild-type protein.

**Conclusions:** These results support a novel role for UNC-33/CRMP in *C. elegans* epidermal development and shed light on how individual amino acid changes cause a loss-of-function in UNC-33.

#### KEYWORDS

embryogenesis, microtubule-associated proteins, molecular dynamics

#### 1 | INTRODUCTION

Developmental Dynamics. 2022;1-13.

Microtubules are a critical cytoskeletal component involved in a wide array of cellular processes, like separating chromatids during cell division, vesicular transport, and cell movement. These different functions are made possible by the growing number of microtubule-associated proteins (MAPs) that have been identified. Some of these proteins act as chaperones, promoting proper tubulin folding, and assembly of  $\alpha$ - and  $\beta$ -tubulin heterodimers. Other proteins regulate the rates of polymerization and depolymerization along the linear protofilaments that form the hollow, cylindrical structure of microtubules. Microtubule-specific motors, accessory

Rachel Prins and Peter Windsor contributed equally to this work.

transport proteins, and crosslinking proteins can add additional layers of functionality. The overall organization and function of microtubules will therefore depend on the complement of these binding proteins that are actively available in a cell at any given time.

The importance of microtubules beyond simple transport in differentiated cell types other than neurons is not as well understood. In cultured mammalian epithelial cells, for example, microtubules have been shown to associate with cadherin-based intercellular adhesions but the functional significance of these interactions is still unclear.4-7 In one study, disrupting microtubules altered the localization and organization of cadherin-catenin adhesive complexes, perturbing cell-cell interactions<sup>6</sup>; however, in other experiments, destabilizing microtubules actually triggered the formation of cadherin-based adhesions through an interaction with p120-catenin.<sup>4</sup> Some of these discrepancies can be partially explained by the use of different cell lines, but the results also indicate that a more complex model may be needed to fully understand the role microtubules have in epithelial tissues. A developmental animal model would be ideal for this purpose since it would allow examination of microtubules and MAPs in cells that are highly dynamic, undergoing significant changes to their shape, position, and interaction with other cells.

The embryonic development of the epidermis in C. elegans has provided a robust genetic model for studying an intact epithelium in a living organism.8 During embryogenesis, the epithelial cells that will become this tissue stop dividing and undergo a series of cell movements and cell shape changes referred to as epidermal morphogenesis. During dorsal intercalation, two rows of dorsal epithelial cells become wedge-shaped and interdigitate with one another. 10 Around the same time, ventral epithelial cells migrate over underlying cells to make contact with their contralateral neighbors, sealing the embryo in an epithelial sheet. 11 At the end of ventral enclosure, both the F-actin and microtubule cytoskeletons form parallel arrays of circumferentially oriented fibers in the dorsal and ventral epithelial cells and a lessorganized meshwork in lateral seam cells. 12 Actomyosinmediated contractions distributed along these cytoskeletal networks drives cell shape changes that shorten the cells along the dorsal-ventral axis while extending along the anterior-posterior axis, elongating the embryo into a long, thin worm four-times its original length.<sup>9,12</sup> Cell adhesions and intact actin and microtubule cytoskeletons are required for epidermal morphogenesis as perturbations cause embryonic lethality and morphological defects. 11,13

Even though the requirement for intact microtubules during *C. elegans* epidermal morphogenesis has been

shown, it is unknown what complement of MAPs control their dynamics or organization. CRMPs have been shown to control microtubule growth by binding to either  $\alpha$ -tubulin/ $\beta$ -tubulin heterodimers<sup>14</sup> or assembled microtubules. 15 Yeast two-hybrid experiments, 16,17 size exclusion chromatography, 16 and crystallization experiments<sup>18</sup> suggest that CRMPs function as tetramers. The unc-33 gene in C. elegans encodes a conserved member of the CRMP/TOAD/Ulip/DRP family, and has been important in elucidating the role of this protein family in neuronal development. 17,19,20 Several alleles of unc-33 demonstrate defects in axonal outgrowth and guidance due to disorganized and overabundant microtubules, resulting in paralyzed and uncoordinated animals. 17,19-21 These animals have also been reported to be shorter and stouter than wild-type animals (dumpy) but with no clear explanation why. Other dumpy animals are associated with alleles that encode defective cuticle proteins<sup>22</sup> but some alleles have been found to be important for proper epidermal morphogenesis, including those of sma-1, 23 let-502, 24 and lin-26. 25 Therefore, we hypothesized that unc-33 may also play a role in epidermal morphogenesis.

C. elegans embryogenesis provides a robust animal model to study formation of an epidermal tissue during dynamic morphogenetic events that depend on both cell adhesions and microtubules. Through 4D differential interference contrast (DIC) microscopy, we find that homozygous mutant embryos of several unc-33 alleles (e204, e572, e1261, and mn407) exhibit defects during epidermal morphogenesis. We have also discovered two missense mutations in homozygous unc-33 (e572) animals, V476G, and S731T, and a nonsense mutation in unc-33(e1261), Q655Amber. To better understand how the missense mutations in e204 and e572 may result in a loss-of-function of UNC-33, we used homology modeling and molecular dynamics (MD) simulations to demonstrate the effects these changes could have on UNC-33 tetramer structure. We find that these amino acid changes result in unique movements when comparing the wild-type and mutant proteins primarily due to changes in intramolecular hydrogen bonding. Free energy calculations also reveal added local stability near the mutation sites on the UNC-33 protein.

#### 2 | RESULTS AND DISCUSSION

The neuronal defects and uncoordinated behavior of adult *C. elegans* harboring *unc-33* mutant alleles have long been recognized but fails to explain the body morphology defect. In this study, we not only examined

epidermal development during embryogenesis of unc-33 mutants, but also identified unknown base substitutions within two of these alleles. To further understand how subsequent missense mutations in UNC-33/CRMP might affect its function, we turned to computational chemistry tools to analyze the UNC-33/CRMP structure.

## 2.1 | Homozygous *unc-33(e204)* embryos take longer to complete epidermal morphogenesis compared to wildtype

To determine if UNC-33/CRMP plays a role in forming the embryonic epidermis in C. elegans, 4D DIC microscopy was used to compare the completion of epidermal morphogenesis between wild-type and homozygous unc-33 mutant animals (Figure 1). In a wild-type embryo, it takes approximately 54 minutes for the epidermal cells that are first seen migrating around the ventral surface of the embryo (Figure 1A; 0 min, white arrow) to complete ventral enclosure and the initial body elongation that results in a 1.25-fold increase in body length (Figure 1B). While homozygous mutants of both unc-33(e572) and unc-33(e1261) also reach 1.25× elongation after 54 minutes from the onset of ventral enclosure (Figure 11,J and M,N, respectively), unc-33(e204) and unc-33(mn407) homozygous mutant embryos lag behind (Figure 1E,F and O.R., respectively), with e204 animals often still completing ventral enclosure (Figure 1F; carets). Similarly, at the time wild-type animals have elongated 1.7-fold their original length (Figure 1C; short-dashed line), homozygous unc-33(e204) and mn407 mutants have only elongated 1.4-fold (Figure 1G,S). Furthermore, it now appears unc-33(e1261) mutants are also lagging behind wildtype, only reaching  $1.5 \times$  elongation (Figure 10) 99 minutes after the onset of ventral enclosure. This trend continues during the next phase of body elongation, where unc-33 (e204) mutants have only reached 1.5× elongation (Figure 1H) and unc-33(e1261) and unc-33(mn407) mutants have only reached 1.8× elongation (Figure 1P,T) when compared to two-fold elongated wild-type animals (Figure 2D; long-dashed line). Unlike the developmental delays observed in unc-33(e204), unc-33(e1261), and unc-33(mn407), homozygous animals from unc-33(e572) appear to develop at a similar pace to wildtype from the onset of ventral enclosure through 2× elongation (Figure 1I-L).

To determine if the progression through epidermal morphogenesis was indeed slower than wildtype, the elapsed time between the onset of ventral enclosure and two-fold body elongation was calculated for at least eight homozygous mutant embryos of each allele (Figure 1U). Only e204 was found to be significantly slower than

wildtype, with a mean interval of  $214 \pm 63.7$  minutes compared to  $136 \pm 14.5$  minutes (P <.01). It is possible that a substage within this interval more greatly affects the total elapsed time; therefore, a subtle defect in one substage could be masked by only examining the larger interval. Several discrete substages were chosen for analysis (Figure 2A-D): the onset of ventral enclosure to completion of ventral enclosure (A), ventral enclosure to 1.25-fold body elongation (B), 1.25-fold to 1.5-fold body elongation (C), and 1.5-fold to 2-fold body elongation (D). These intervals were chosen based on the changing functions of epidermal cells over developmental time<sup>9</sup>; for example, cells migrating during ventral enclosure vs cells initiating contraction as the animal elongates to 1.25-fold. Elongation between 1.5-fold and 2-fold may be impacted by active body wall muscle compared to muscleindependent elongation between 1.25-fold and 1.5-fold. However, the only allele to demonstrate a significant lag across these smaller intervals was e204 (Figure 2A,C,D) except for the interval between completion of ventral enclosure and 1.25× elongation (Figure 2B).

## Strong loss-of-function *unc-33* alleles exhibit significant embryonic lethality

In order to analyze timing differences during epidermal morphogenesis between the *unc-33* alleles (Figures 1 and 2), it was necessary to examine embryos that at least made it to two-fold body elongation. However, some homozygous unc-33 mutant embryos either never developed to the onset of ventral enclosure, halted prior to reaching two-fold elongation, or even ruptured as the animal began to elongate (Figure 3). Together, these three phenotypes were regarded as embryonic lethal since the animals do not hatch from the eggshell. When compared to the proportion of progeny that elongated to at least two-fold and typically hatched, wildtype and e204 had the lowest percentage of embryonic lethality (Table 1) and were not statistically different from each other. The other three *unc-33* alleles were all significantly different from e204 (e1261, P = .01; e572, P = .03; mn407, P = .02), but not amongst themselves. Only e1261 was significantly different from wildtype (P = .03; e572, P = .09; mn407, P = .06). Embryonic lethality is highest in the strong loss-of-function allele e1261 (21.35%) compared to the weak loss-of-function allele e204 (1.64%), which is consistent with previous studies that found a higher percentage of axonal outgrowth defects in D-type motoneurons in null alleles compared to e204.<sup>17</sup> With respect to the lethal phenotypes, a similar allelic series to defects in neuronal development<sup>17</sup> is observed in this

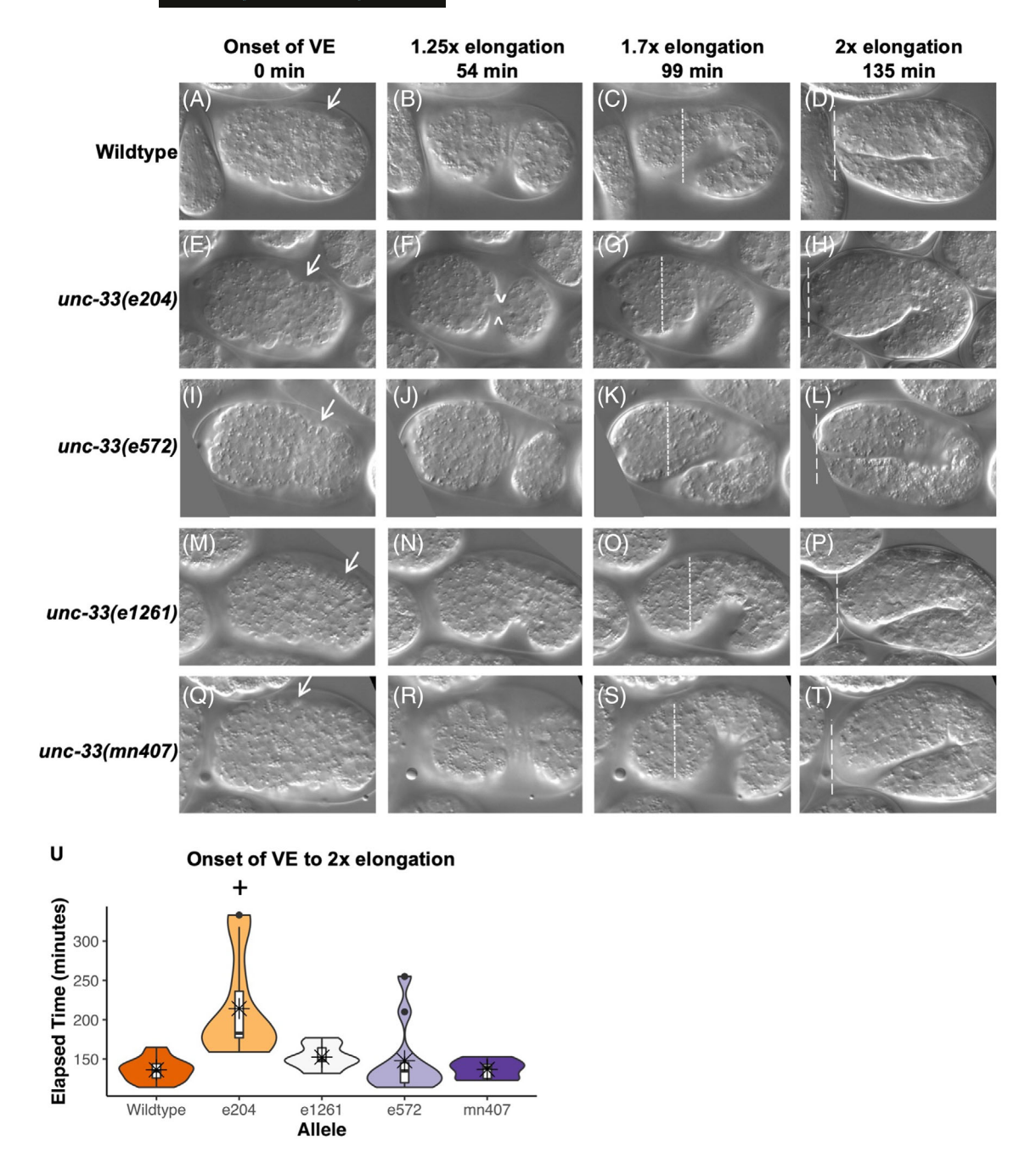
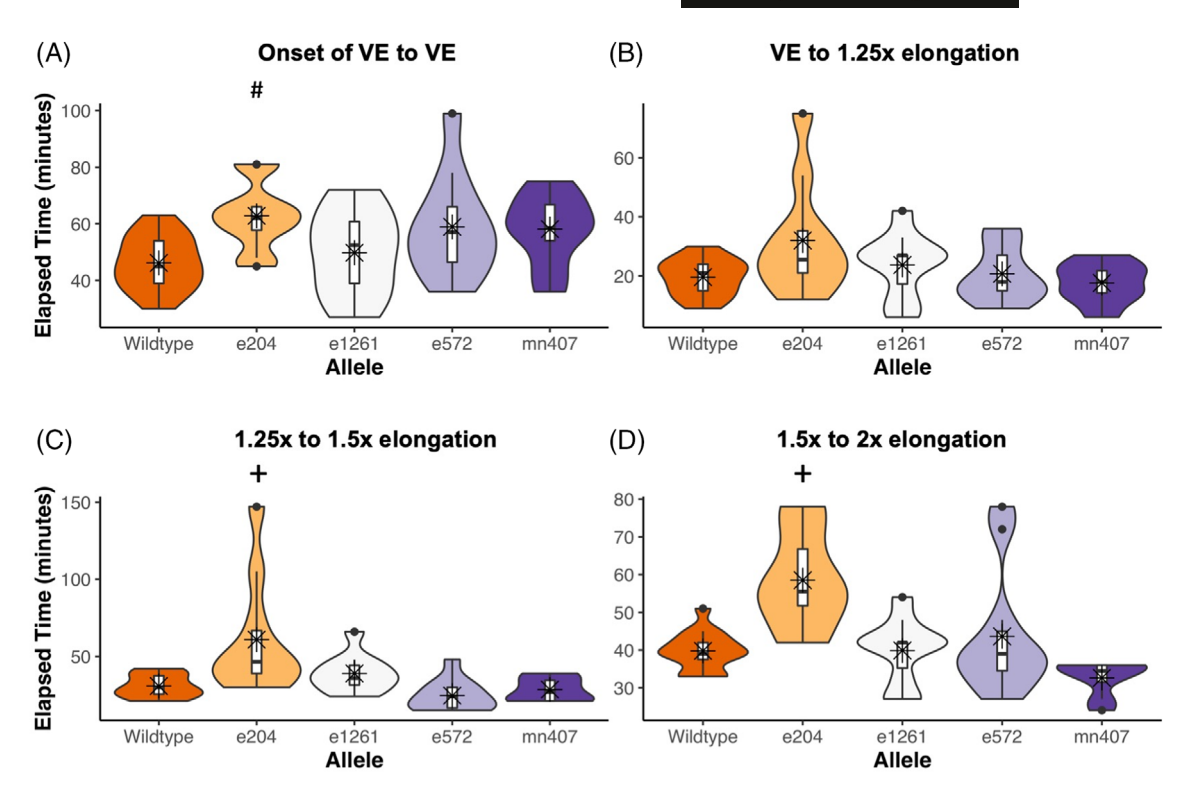


FIGURE 1 Homozygous unc-33(e204) embryos take longer to complete epidermal morphogenesis compared to wild-type. (A-T) Time-lapse series of DIC micrographs for wild-type and four unc-33 alleles. Arrows indicate first lateral glimpse of cells migrating toward the ventral midline. Carets indicate incomplete ventral enclosure. Short dashed line indicates expected 1.7-fold embryo length. Long dashed line indicates expected two-fold embryo length. (U) Total elapsed time between the onset of VE and two-fold body elongation. Horizontal bar = median. Asterisk = mean. Box limits indicate the 25th and 75th percentiles; whiskers extend 1.5 times the interquartile range. Outliers are represented by black circles. Plus sign = P < .01 based on one-way ANOVA and Tukey's HSD. From left to right, the number of embryos examined for each strain = 15, 10, 10, 11, and 8.

study: e204 < e572 < mn407 < e1261. Interestingly, the two putative null alleles, unc-33(mn407) and unc-33 (e1261), were the only two that exhibited ruptures (Figure 3C,D, and G,H; arrows) even though progression through epidermal morphogenesis was similar to wildtype (Figures 1 and 2).

The *e204* allele confers a missense mutation of an aspartate to an asparagine at amino acid 389 of isoform A (Table 2).<sup>17</sup> One mechanistic explanation for the developmental delay exhibited by *e204* animals is simply defective microtubule transport, which could cause the process to slow but not entirely fail. Neurons in *unc-33* 



**FIGURE 2** Development of homozygous unc-33(e204) embryos is slowed throughout epidermal morphogenesis. (A-D) Elapsed time between specific developmental landmarks. Horizontal bar = median. Asterisk = mean. Box limits indicate the 25th and 75th percentiles; whiskers extend 1.5 times the interquartile range. Outliers are represented by black circles. Plus sign = P < .01 and pound sign = P < .05 based on one-way ANOVA and Tukey's HSD. From left to right, the number of embryos examined for each strain = 15, 10, 10, 11, and 8.

mutants have over twice as many microtubules as wildtype that are sometimes wider with inappropriate hooks or doublet or triplet structures. 19 Microtubules in the epidermis during epidermal morphogenesis are highly organized, as noted earlier. Too many microtubules could negatively affect directed microtubule-based transport of key molecules to specific cellular locations, like adherens junctions. HMP-2/β-catenin is an important adherens junction protein that binds both the transmembrane cadherin and the actin-binding protein HMP-1/ $\alpha$ -catenin. A genetic interaction between hmp-2/β-catenin and unc-33/CRMP during C. elegans embryonic development was recently reported, which could support this hypothesis.<sup>28</sup> The ruptured embryos observed in the strong loss-offunction mutants, e1261 and mn407 (Figure 3), could be demonstrating the difference between a lack of UNC-33 protein and dysfunctional protein.

It is important to note that there is the possibility that one or more of the strains used in this study harbors additional mutations outside of *unc-33*. Future experiments are aimed at determining if the phenotypes reported here are in fact specific to perturbation of *unc-33* and whether or not they are due to epidermal cell dysfunction during development.

# 2.3 | *unc-33(e572)* encodes two missense mutations while *unc-33(e1261)* encodes a nonsense mutation

The mutations in both unc-33(e572) and unc-33(e1261) alleles were mapped to the unc-33 locus but the exact DNA lesion is still unknown. 17,20 Since we observed differences in the effects of unc-33 alleles on the progression of epidermal morphogenesis (Figures 1 and 2) and embryonic lethality (Table 1 and Figure 3), we wanted to better understand how the function of UNC-33 protein could be affected by specific amino acid changes. Using a TOPO-TA cloning strategy with subsequent Sanger sequencing, we compared the unc-33 genomic region in e572 and e1261 homozygous mutant animals to wild-type reference sequences and identified possible changes in the UNC-33 primary sequence for both alleles. Surprisingly, two changes were found in the genomic sequence of unc-33(e572) (Table 2). The first is a transversion in the coding strand of exon 8 (Figure 4), conferring a valine to glycine missense mutation at amino acid 476. The second is also a transversion but in the coding strand of exon 9 (Figure 4), conferring a serine to threonine missense mutation at amino acid 731.

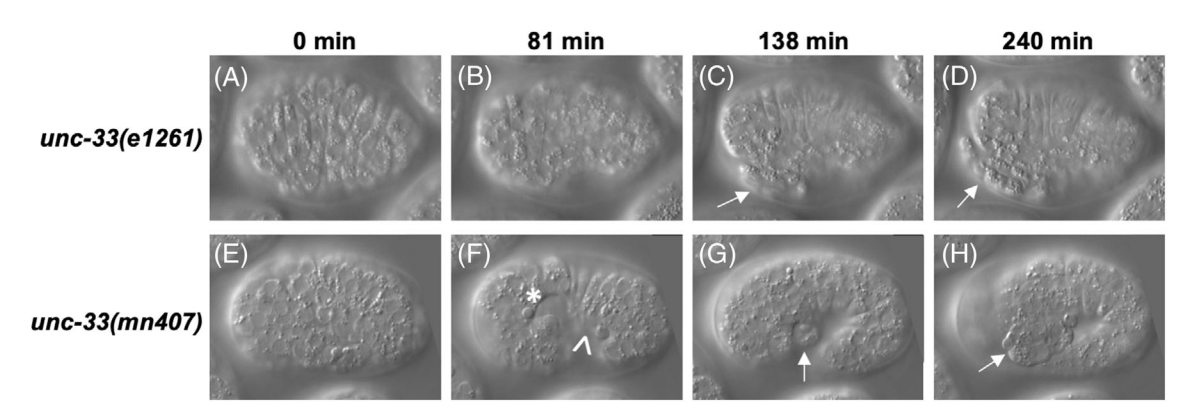


**FIGURE 3** Homozygous embryos of null *unc-33* alleles exhibit rupturing during epidermal morphogenesis. (A-H) Time-lapse series of DIC micrographs for *unc-33(e1261)* and *unc-33(mn407)*. Arrows = rupturing cells. Caret = attempted ventral enclosure. Asterisk = opening left by incomplete ventral enclosure.

**TABLE 1** Percentage of embryonic lethality noted among *unc-33* alleles.

Strain	Allele	Embryonic lethal	2× elongation or greater	Total embryos	Percent embryonic lethal
N2	_	4	78	82	4.88
CB204	unc-33(e204)	1	60	61	1.64
CB1261	unc-33(e1261)	19	70	89	21.35*
CB572	unc-33(e572)	23	103	126	18.25
SP1382	unc-33(mn407)	26	109	135	19.26

*Note*: Any embryo that did not make it to two-fold body elongation and failed to hatch was regarded as embryonic lethal. "\*" = P < .05 when compared to wild-type (chi-square test of independence; Bonferroni correction). When compared to e204, all other unc-33 alleles were statistically different (P < .05).

TABLE 2 Base substitutions identified in unc-33 alleles result in amino acid changes to UNC-33/CRMP.

Strain	Allele	Codon change	UNC-33, isoform A, amino acid change	Human CRMP-2 residue
	unc-33(e204)		Asp389Asn <sup>17</sup>	Asp176
	unc-33(tr114)		Arg502His <sup>21</sup>	Gln310
CB572	unc-33(e572)	GTG → GGG	Val476Gly	Leu270
CB572	unc-33(e572)	$TCA \rightarrow ACA$	Ser731Thr	Ser533
CB1261	unc-33(e1261)	CAG → TAG	Gln655Amber	Pro457

*Note*: Shaded rows indicate alleles with previously published missense mutations. The amino acids in human CRMP-2 that are equivalent to those changed in UNC-33 were identified through a multiple sequence alignment (data not shown).<sup>26,27</sup>



**FIGURE 4** The genomic location of point mutations in sequenced *unc-33* alleles. Black boxes indicate exons while connecting lines indicate introns. Green star = e204 allele. Scale bar = 100 base pairs.

This particular change is consistent with a previous report of a polymorphism in a SacI recognition site within exon 9 of e572.<sup>20</sup> There is no evidence that S731

is phosphorylated in CRMPs, but S731 is in a region of the CRMP family of proteins predicted to be a C-terminal microtubule binding domain (CMBD).<sup>15</sup>

Previous work has shown that *unc-33(e1261)* homozygous mutant animals do not express any of the three main isoforms of UNC-33 protein when analyzed by immunoblot with two different polyclonal antibodies.<sup>17</sup> The discovery of a premature stop codon, Gln655Amber (Table 2), is consistent with this if nonsense-mediated decay mechanisms are removing aberrant transcripts or if this truncation results in a severely destabilized protein structure that is rapidly degraded.

For both *unc-33(e1261)* and *unc-33(e572)*, there was an approximately 220 base pair region of intron 8 that had no sequence coverage and a 400 base pair region of the next exon (9) that had less than three independent reads in some areas despite clones containing that portion of the genome. Polynucleotide sequences in the area are likely causing the issue despite the use of multiple upstream and downstream primers. Because wild-type-sized transcripts for the three main isoforms was confirmed in *unc-33(e572)*,<sup>20</sup> it is unlikely any potential mutations in this area would cause additional amino acid changes. While transcript data have not been shown for *unc-33(e1261)*, the lack of protein product means it is likely behaving as a null allele.

Neither of the missense mutations in *unc-33(e572)* homozygous mutant animals is drastic when you compare the chemistry of the amino acids. Because it is not obvious how missense changes might affect UNC-33/CRMP structure or function, computational modeling methods were used for further investigation.

# 2.4 | Analysis of MD simulations reveals changes to hydrogen bonding between wild-type and mutant UNC-33/CRMPs

MD simulations have emerged as a beneficial tool in elucidating the effects of amino acid mutations, allowing for the atomistic behavior of the protein to be monitored.<sup>29-31</sup>

Here, MD simulations were used to investigate the D389N change in *unc-33(e204)*, R502H in *unc-33(tr114)*, and the newly discovered amino acid mutations, V476G and S731T, found in *unc-33(e572)*. The structure of *C. elegans* UNC-33/CRMP was generated through homology modeling due to the *C. elegans* protein currently being unsolved. Human CRMP-4 (PDB: 4CNT)<sup>18</sup> was used as the model as it is one of the few available structures with >36% amino acid sequence similarity to C. elegans UNC-33/CRMP. The majority of the N-terminus for each monomer was unable to be modeled because of the absence of corresponding residues in the reference crystal structure. Additionally, it should be noted that human CMRP-4 also shares a high sequence similarity (~50%) with the two other proteins in the

*C. elegans* dihydropyrimidinase family. If the structural locations of V476 and S731 are compared in our homology model, V476 is embedded within each monomer similar to D389 and R502, while S731 is on the surface of each folded monomer in the tetramer (data not shown).

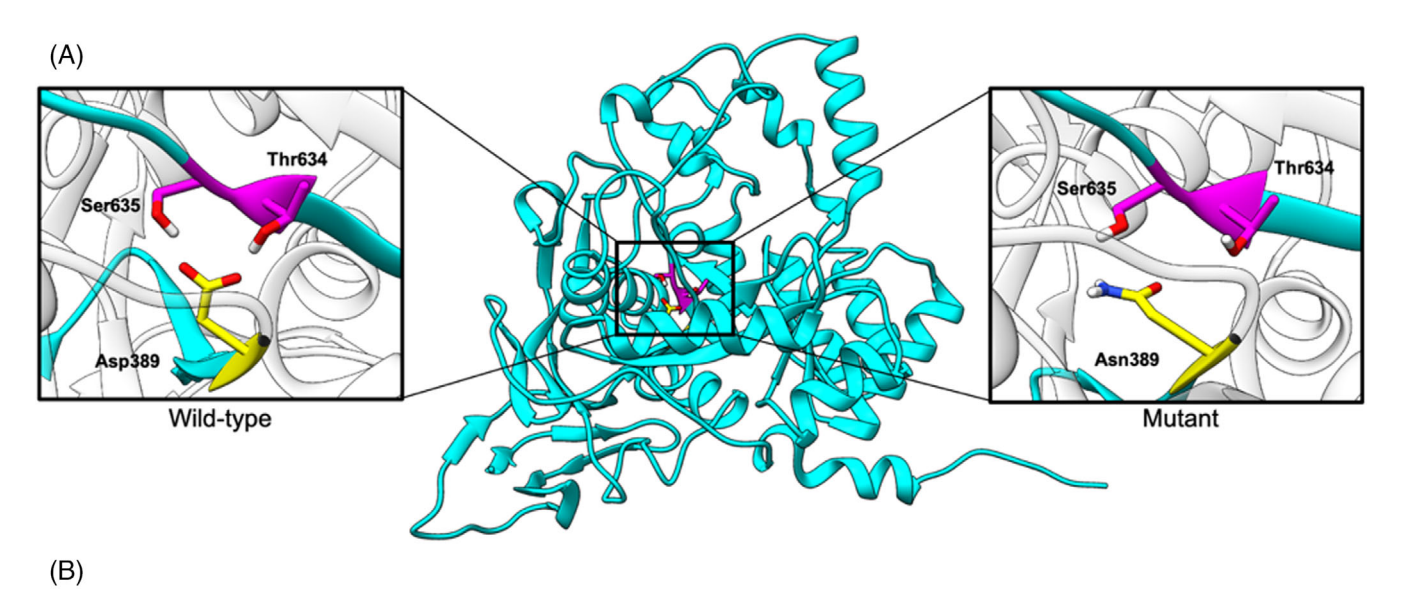
Equivalent amino acid mutations were generated in each monomer of the tetrameric structure, and explicit solvent unrestrained MD was performed on the wild-type and mutant proteins. The V476G/S731T mutant was simulated as one double mutation and two single mutations (V476G and S731T). The single mutation simulations showed similar behavior to the double mutation (data not shown), so the double mutation will be analyzed here to accurately represent the allele that was sequenced. The simulations were performed over a 1.5  $\mu s$  timescale. Analyses of mutant protein trajectories reveal disruption of intramolecular hydrogen bonding networks that lead to local structural and energetic changes suggesting a mechanism for protein dysfunction.

#### 2.4.1 | Global structural analysis

Root mean square deviation (RMSD) of the  $C_{\alpha}$  atoms was used to measure the conformational stability over the course of a simulation. Both the wild-type and the mutant structures showed minimal deviation from the respective starting structure over the simulation (data not shown). Root mean square fluctuation (RMSF) of the  $C_{\alpha}$ atoms was used as a measure of the dynamics of each residue in the structure, with the RMSF for each residue being averaged across each of the four monomers. No significant differences in fluctuation were observed between the wild-type and mutants, specifically at the mutation sites (data not shown). Minimal deviation between the wild-type and mutants is likely due to the highly structured and rigid qualities of the protein. Due to this observation, hydrogen bond analysis, and free energy decomposition analysis were employed to investigate how mutations affected the local protein environment.

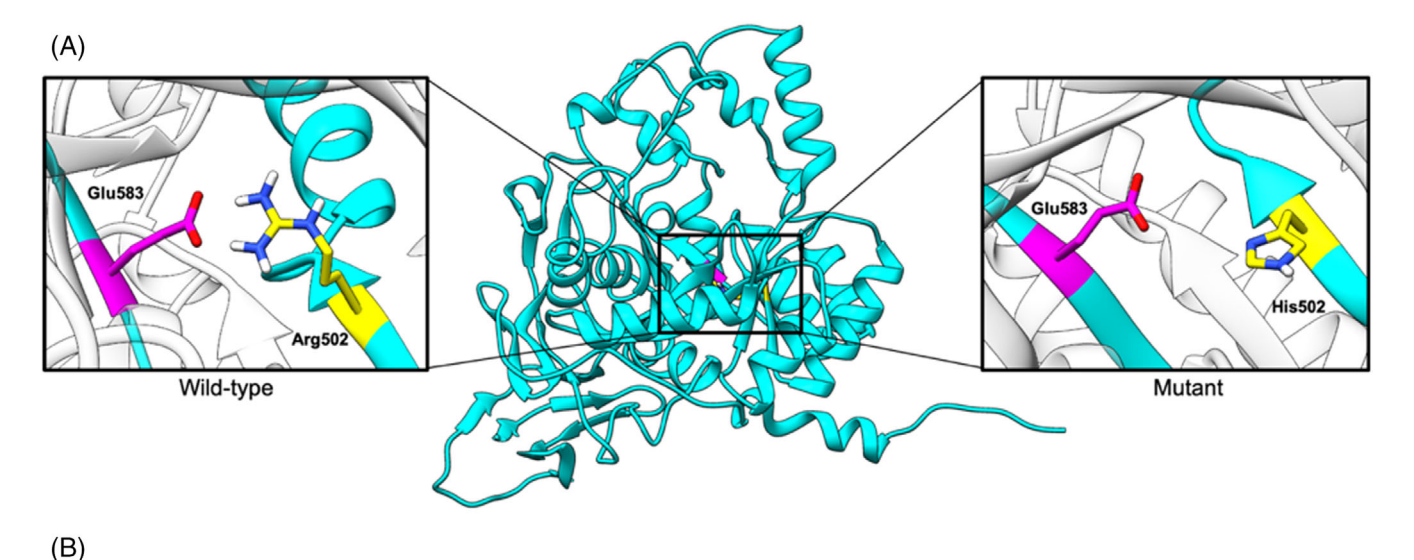
#### 2.4.2 | Local structural analysis

Visual analysis of the wild-type and mutant MD trajectories revealed that mutations affect local hydrogen bonding and structural interactions. Specifically, D389N (Figure 5) and R502H (Figure 6) mutations perturbed protein-protein hydrogen bonds that were observed in the wild-type. These changes can be attributed to the spatial and chemical nature of these mutations. The replacement of a hydrogen bond acceptor with the hydrogen bond donating ability of the D389N mutation causes the



Trajectory	389 to 635	389 to 634	389 to Solvent	635 to Solvent	634 to Solvent
Wild-type (%)	100.0	39.9	0.0	0.0	2.2
D389N (%)	0.0	0.0	46.8	56.9	62.5

FIGURE 5 Local structural analysis of UNC-33 D389N missense mutation. (A) 3D ribbon representation of UNC-33/CRMP monomer (middle). Atomic representation of local structure for wild-type (left) vs D389N mutant (right) with respective point mutation highlighted in yellow. (B) Local hydrogen bond occupancies of the residues near the mutation site. Residues form hydrogen bonds with solvent upon mutation.



(-)					
Trajectory	502 to 583	502 to 474	560 to 583	502 to Solvent	583 to Solvent
Wild-type (%)	94.0	0.9	9.1	0.0	0.0
R502H (%)	7.9	18.1	51.4	91.0	94.2

FIGURE 6 Local structural analysis of UNC-33 R502H missense mutation. (A) 3D ribbon representation of UNC-33/CRMP monomer (middle). Atomic representation of local structure for wild-type (left) vs R502H mutant (right) with respective point mutation highlighted in yellow. (B) Local hydrogen bond occupancies of the residues near mutation site. Residues form hydrogen bonds with solvent upon mutation.

Asn389 to adopt a conformation that is not suitable to participate in hydrogen bonding present in the wild-type (Figure 5). Additionally, the R502H mutation drastically

reduces the length of the amino acid side chain at the 502 position, which prevents a hydrogen bond from occurring (Figure 6). In order to supplement these

changes, the amino acids formed hydrogen bonds with the solvent. Hydrogen bond interactions were quantified by calculating the percentage of time hydrogen bonds persisted throughout the simulations (Figures 5B and 6B). It is evident that the D389N and R502H mutations cause a decrease in protein-protein hydrogen bonds and an increase in protein-solvent hydrogen bonds relative to the wild-type. The V476G/S731T mutations were not observed to change local interactions in CRMP (data not shown) as these mutations are less chemically severe compared to R502H and D389N. No significant local hydrogen bond changes were observed at the site of the V476G mutation (data not shown). Additionally, the S731T mutation did not drastically change local proteinprotein or protein-solvent hydrogen bonding (data not shown).

Per-residue free energy decomposition calculations were used in order to investigate the energetic effects of these mutations. Total free energy changes were decomposed into  $\Delta G_{\rm int}$ ,  $\Delta G_{\rm vdw}$ ,  $\Delta G_{\rm ele}$ ,  $\Delta G_{\rm p}$ , and  $\Delta G_{\rm np}$ (see Table 3 caption for definitions) to determine which energy component was affected most by the mutations. At the D389N mutation site (Table 3), increased stability (more negative free energy) was observed upon mutation from aspartate to asparagine. This increase in stability is mainly attributed to  $\Delta G_{\rm int}$  and  $\Delta G_{\rm ele}$ . The large decrease in  $\Delta G_{\rm int}$  is likely due to asparagine being more flexible and mobile since it is not dynamically restrained by protein-protein hydrogen bonding. Additionally, the increase in bonds, angles, and dihedrals in asparagine increases the number of microstates available to the residue which increases entropy and lowers free energy. The decrease in  $\Delta G_{\rm ele}$  is likely a result of an increase in the number of hydrogen bonding partners of the asparagine relative to the aspartate. Although the mutant asparagine does not interact with the same side chains as the wildtype (Thr634 and Ser635), it does form significant

intermolecular hydrogen bonds with several other amino acids (eg, backbone of Val418 and Thr416 and side chain of Tyr391) in addition to the increased hydrogen bonding with solvent. The surrounding residues showed minimal energetic changes upon mutation which is likely due to the residues forming interactions with solvent as opposed to the protein.

The R502H mutation site was less stable relative to the wild-type, and this change can be largely attributed to  $\Delta G_{\rm int}$  (data not shown). Upon mutation from an arginine to a histidine, bonds, angles, and dihedral angles decreased flexibility, which decreased entropy (available microstates) and ultimately increased free energy. Minimal energetic changes were observed at the V476G mutation site and at local residues around the V476G and S731T mutation sites (data not shown). The S731T mutation increased stability at the mutation site, which can also be attributed to  $\Delta G_{\rm int}$  (data not shown) for the reasons outlined above.

#### 3 CONCLUSION

We have shown that homozygous mutant embryos of unc-33(e204) progress more slowly through C. elegans epidermal morphogenesis, while those of e572, e1261, and mn407 exhibit a higher percentage of embryonic lethality, including rupturing during epidermal morphogenesis. These results demonstrate a previously unknown role of UNC-33 in epidermal morphogenesis. MD simulations predict that the D389N and R502H missense mutations disrupt hydrogen bond networks leading to structural and energetic perturbations in the CRMP structure. We hypothesize that these changes interfere with protein-protein interactions during microtubule formation. Future in vivo experimentation will aim to test this hypothesis as well as to identify novel protein

Per-residue free energy decomposition for local environment of wild-type and D389N mutation. TABLE 3

Trajectory	Residue	$\Delta G_{ m int}$ (kcal mol $^{-1}$ )	$\Delta G_{ m vdw} \ ({ m kcal~mol}^{-1})$	$\Delta G_{ m ele} \ ({ m kcal}{ m mol}^{-1})$	$\Delta G_{ m p}$ (kcal mol $^{-1}$ )	$\Delta G_{ m np} \ ({ m kcal~mol}^{-1})$	$\Delta G_{ m tot}$ (kcal mol $^{-1}$ )
Wild-type	Asp389*	$116.82 \pm 0.02$	$-7.62 \pm 0.01$	$-65.12 \pm 0.03$	-102.71 ± 0.09	$0.013 \pm 0.001$	$-58.61 \pm 0.02$
	Thr634	$46.42 \pm 0.06$	$-9.03 \pm 0.09$	$-60.83 \pm 0.04$	$-2.72 \pm 0.06$	$0.019 \pm 0.002$	$-6.38 \pm 0.08$
	Ser635	$64.64 \pm 0.01$	$-7.47 \pm 0.04$	$-60.74 \pm 0.09$	$0.17 \pm 0.09$	$0.020 \pm 0.001$	$-23.81 \pm 0.04$
D389N	Asn389*	$40.15 \pm 0.04$	$-10.03 \pm 0.06$	$-98.86 \pm 0.07$	$-3.34 \pm 0.01$	$0.014 \pm 0.009$	$-71.81 \pm 0.07$
	Thr634	$41.97 \pm 0.09$	$-8.01\pm0.01$	$-54.87 \pm 0.01$	$-5.89 \pm 0.01$	$0.023 \pm 0.004$	$-2.85 \pm 0.07$
	Ser635	$64.93 \pm 0.07$	$-8.98 \pm 0.01$	$-52.28 \pm 0.01$	$-1.50\pm0.03$	$0.021 \pm 0.006$	$-21.84 \pm 0.01$

Note: Values are averaged out across each of the four monomers. (±) represents SE of the mean. (\*) represents the residue that was mutated. Important energy changes are highlighted. There are five components contributing to the calculated MM/GBSA free energies: internal energy ( $\Delta G_{int}$ ) van der Waals energy  $(\Delta G_{\text{vdw}})$ , electrostatic energy  $(\Delta G_{\text{ele}})$ , polar solvation energy  $(\Delta G_{\text{p}})$ , and nonpolar solvation energy  $(\Delta G_{\text{np}})$ .

interactions that may provide a mechanistic model of UNC-33 function in the embryonic epidermis. No significant structural or energetic changes were observed in the V476G/S731T mutant simulations. As previously noted, simulations did not contain the N-terminal residues of each monomer due to a lack of crystal structure. It is possible that these mutations perturb these missing residues and cause changes that were unobservable in the simulations. The embryonic lethality observed in unc-33(e572) homozygous animals could be explained by the solvent exposed nature of the S731T mutation site and the predicted location of the CMBD. Obtaining a complete UNC-33/CRMP structure could lead to future MD studies that offer even greater insights into the effect of these mutations on UNC-33 function. Additionally, verifying the precise location of the CMBD would allow for further investigation into how these amino acid changes perturb UNC-33-microtubule interaction on a molecular level.

#### 4 | EXPERIMENTAL PROCEDURES

#### 4.1 | C. elegans strains and alleles

All strains were cultured using standard protocols.<sup>32</sup> The Bristol strain N2 was used as wildtype. Additional homozygous mutant strains used include CB204 [*unc-33* (*e204*)], CB572 [*unc-33*(*e572*)], and CB1261 [*unc-33* (*e1261*)]. These strains were obtained from the CGC and used as is. A strain carrying *unc-33*(*tr114*) was obtained [trIs25;rrf-3(pk1426) (trIs25; rol-6, him-4p::MB::YFP, F25B3.3::dsRed)] but grew very poorly and could not be maintained long enough to outcross or perform sufficient 4D DIC microscopy.

#### 4.2 | Allele sequencing

Individual homozygous *unc-33* mutant adults were transferred to 5 μL of worm lysis buffer [50 mM KCl, 10 mM Tris-HCl pH 8.3, 2.5 mM MgCl<sub>2</sub>, 0.45% NP40, 0.45% Tween 20, 60 μg/mL Proteinase K] and frozen for 15 min at 80°C, lysed at 65°C for 1 hour, incubated at 95°C for 15 min, then kept on ice until use. Genomic *unc-33* DNA was amplified in several overlapping fragments using Phusion polymerase [Thermo Fisher, F530S] in a 20 μL PCR containing 5 μL worm lysate and 5% DMSO. Fragments of *unc-33* were created with the following primer sets: RP1-FWD [GCAAAATACACATTTATCACTAGA GGAGGG] and RP15-REV [CCACTCAAATTTGATG TGAAATCGAGC]; RP6-FWD [CCCAATATTTGGAG CTTTCAGGCC] and RP16-REV [CGTAATCGCCAC AGAAAGTGCC]; RP9-FWD [GCTATTTTATCAACA

AAACACTGTAAACTCC] and RP17-REV [GCTACCA AAACCCTGTAGTCCG]. Products were incubated with Taq polymerase [Invitrogen, 10342053] for 15 minutes at 72°C to add A-overhangs. DNA was purified (Promega, A9282) and cloned using the TOPO-TA Cloning Kit for Sequencing (Invitrogen, 450030) and transformed into DH5α competent cells [Invitrogen, 18265017]. Individual clones were miniprepped (Promega, A1460) and sequenced through Eurofins Genomics. Each region of the genome was sequenced from at least three individual worms using the following primers: RP2: GGATACG AAAAGTCGCAATGTTCAGG, RP3: GCAGAATTTTT TACAGAACTACCCCC, RP4: GCAAAAAGTGTAATT TTCCACTTTTCGTGG, RP5: CGTCAAAAATGCTCAA ATTGTCAATGACG, RP7: GCTCGATTTCACATCAA ATTTGAGTGG, RP8: GGTGTATCTCAAAATCTCTGAA CAAATCC, RP10: GGCACTTTCTGTGGCGATTACG, RP11: CCACAAAAAATCCCGGAAATCCC, RP12: GCC TATCAGAATGGAGAAGTTCGGG, RP13: CGTTTTA CAGTTCGCCAACGTGG, RP14: CGTGATGGGACA ACCTGAAACC, RP20: GGTGGTTTGTACGTCCGGAC ATCG, RP21: GGAGTTTACAGTGTTTTGTTGATAAA ATAGC, RP22: CCACGTTGGCGAACTGTAAAACG, T3: ATTAACCCTCACTAAAGGGA, T7: TAATACGACTCA CTATAGGG.

### 4.3 | Microscopy

4D DIC microscopy was used to determine the elapsed time between various developmental stages during embryonic epidermal morphogenesis. Embryos were isolated from gravid hermaphrodites, mounted on a 5% agarose slide, and imaged using 1- $\mu$ m slice spacing throughout the embryo at 3-minute intervals over 9 hours using a Leica DIC microscope with a 63×/1.25 NA oil HCX PL FLUOTAR objective at 20°C with a Windows PC computer running IPLab 4.0 software and a Qimaging QICAM Fast 1394 camera. For determining embryonic lethality, embryos were mounted in the same way but only two still images were taken at time = 0 and time  $\geq$  21 hours.

#### 4.4 | Statistical analyses

A one-way ANOVA with post hoc Tukey analysis using R Studio was used to determine the statistical significance of differences in elapsed time between various developmental stages when comparing wild-type and homozygous *unc*-33 mutant embryos. Plots for examining normality and homoscedasticity revealed several outliers, which were examined for their influence on the data.

Several outliers across different intervals were from the same embryo, which was found to affect the conclusions for at least one interval. The data from this one embryo was therefore removed. Basic summary statistics and violin plots were also created using R Studio.

To determine the significance of the embryonic lethality observed across the *unc-33* alleles, a chi-square test of independence was performed in R Studio (P = .0002998) with subsequent pairwise comparisons with Bonferroni corrections ( $\alpha = .05$ ).

# 4.5 | Generation of homology model and mutant structures

Swiss Model was used to create a homology model of UNC-33 tetramer using the solved crystal structure of human CRMP-4 (PDB: 4CNT). The amino acid sequence used for the model was obtained from the genome database Wormbase (UNC-33, isoform A; 854 amino acids). The first 334 residues of the N-terminal tail for each monomer were unable to be generated due to an absence of corresponding residues in the reference crystal structure. The RMSD for the homology model and original PDB structure was found to be 0.855 Å. Prior to simulation, in silico mutations were generated in each monomer of the wild-type starting structure.

#### 4.6 | MD simulations

Explicit hydrogen atoms were added to the protein and its mutant structures using the tleap module of AmberTools.<sup>35</sup> Proteins were solvated in a truncated octahedron unit cell with TIP3P water molecules with a 12.0 Å solvent buffer between the protein and the closest edge of the unit cell.<sup>36</sup> In vivo conditions were recreated by adding Na<sup>+</sup> ions for a concentration of 0.150 M, and the system was neutralized by adding Cl<sup>-</sup> counter ions. Additionally, the ff14SB force field was applied to the protein.<sup>37</sup> The GPU-accelerated *pmemd* code of Amber16 was used to perform all steps of MD for each system. 38,39 Each system underwent a seven-step minimization process consisting of a maximum of 1000 steps of steepest descent minimization followed by a maximum of 5000 steps of conjugate gradient minimization for each step. For the first step of minimization, all solute heavy atoms were subjected to restraints starting at 10.0 kcal/mol/Å<sup>2</sup>. Restraints were lowered systematically over the course of each step with the last step having a restraint of 0.0 kcal/ mol/Å<sup>2</sup>. Next, the system was heated linearly from 10.0 to 293.0 K over 2.0 ns. During heating, all solute atoms were subjected to a restraint of 10.0 kcal/mol/Å<sup>2</sup>. A

maximum temperature of 293.0 K was chosen in an effort to mimic the conditions at which the experimental trials were completed. Equilibration of the system was carried out over 3.5 ns at a constant temperature of 293.0 K. All solute heavy atoms were subjected to restraints of 10.0 kcal/mol/Ų for the first 0.5 ns, and restraints were decreased systematically every 0.5 ns until reaching a restraint weight of 0.0 kcal/mol/Ų for the final 0.5 ns. After equilibration of the system, unrestrained MD was performed at a constant pressure of 1 atm and constant temperature of 293.0 K. The coordinates were saved every 100 ps, and all systems were simulated without restraints for 1500 ns.

### 4.7 | MD analysis

MD analysis (RMSD, RMSF, and hydrogen bond analysis) was performed using the *cpptraj* module of Amber16.<sup>40</sup> The visualization of the completed trajectories was carried out using visual molecular dynamics and Chimera.<sup>41,42</sup>

#### 4.8 | Free energy decomposition analysis

To analyze free energies of each residue for the individual systems, the free energy decomposition of the wild-type and mutants were computed using the Molecular Mechanics/Generalized Born Surface Area (MM/GBSA) approach. There are five components contributing to the calculated MM/GBSA energies: internal energy ( $\Delta G_{\rm int}$ ) van der Waals energy ( $\Delta G_{\rm vdw}$ ), electrostatic energy ( $\Delta G_{\rm ele}$ ), polar solvation energy ( $\Delta G_{\rm p}$ ), and nonpolar solvation energy ( $\Delta G_{\rm np}$ ). Energy calculations were performed every frame for a total of 15 000 frames per simulation. Free energy decomposition calculations were completed on a per-residue basis for each simulation.

#### **AUTHOR CONTRIBUTIONS**

Rachel Prins: Formal analysis (lead); investigation (lead); validation (equal); visualization (equal); writing – original draft (equal); writing – review and editing (supporting). Peter Windsor: Formal analysis (lead); investigation (lead); validation (equal); visualization (equal); writing – original draft (equal); writing – review and editing (equal). Bill R. Miller III: Conceptualization (equal); funding acquisition (equal); methodology (equal); project administration (equal); resources (equal); supervision (equal); writing – original draft (equal); writing – review and editing (equal). Stephanie Maiden: Conceptualization (equal); formal analysis (supporting); funding acquisition (equal); investigation (supporting);

methodology (equal); project administration (equal); resources (equal); supervision (equal); validation (supporting); writing – original draft (equal); writing – review and editing (equal).

#### **ACKNOWLEDGMENT**

Some strains were provided by the CGC, which is funded by National Institutes of Health Office of Research Infrastructure Programs (P40 OD010440).

#### CONFLICT OF INTEREST

The authors declare no potential conflict of interest.

#### DATA AVAILABILITY STATEMENT

The genomic nucleotide changes sequenced from *unc-33* (e572) and *unc-33*(e1261) homozygous animals will be submitted to *Wormbase.org* for curation.

#### ORCID

Stephanie Maiden https://orcid.org/0000-0002-5144-386X

#### REFERENCES

- Alfaro-Aco R, Petry S. Building the microtubule cytoskeleton piece by piece. J Biol Chem. 2015;290(28):17154-17162. doi:10. 1074/jbc.R115.638452
- Tian G, Lewis SA, Feierbach B, et al. Tubulin subunits exist in an activated conformational state generated and maintained by protein cofactors. *J Cell Biol.* 1997;138(4):821-832. doi:10.1083/ jcb.138.4.821
- 3. Akhmanova A, Steinmetz MO. Control of microtubule organization and dynamics: two ends in the limelight. *Nat Rev Mol Cell Biol.* 2015;16(12):711-726. doi:10.1038/nrm4084
- Maiden SL, Petrova YI, Gumbiner BM. Microtubules inhibit Ecadherin adhesive activity by maintaining phosphorylated p120-catenin in a colon carcinoma cell model. *PLoS One.* 2016; 11(2):1-18. doi:10.1371/journal.pone.0148574
- Meng W, Mushika Y, Ichii T, Takeichi M. Anchorage of microtubule minus ends to adherens junctions regulates epithelial cell-cell contacts. *Cell.* 2008;135(5):948-959. doi:10.1016/j.cell. 2008.09.040
- Stehbens SJ. Dynamic microtubules regulate the local concentration of E-cadherin at cell-cell contacts. *J Cell Sci.* 2006; 119(9):1801-1811. doi:10.1242/jcs.02903
- Shahbazi MN, Megias D, Epifano C, et al. CLASP2 interacts with p120-catenin and governs microtubule dynamics at adherens junctions. *J Cell Biol.* 2013;203(6):1043-1061. doi:10.1083/jcb.201306019
- 8. Hsiao TI, Chisholm AD. The *C. elegans* epidermis as a model skin. I: development, patterning, and growth. *Wiley Interdiscip Rev: Dev Biol.* 2012;1(6):861-878. doi:10.1002/wdev.79
- 9. Chisholm AD, Hardin J. Epidermal Morphogenesis. WormBook: the online review of C elegans biology; 2005; 1-22. doi:10.1895/wormbook.1.35.1
- Williams-Masson EM, Heid PJ, Lavin CA, Hardin J. The cellular mechanism of epithelial rearrangement during

- morphogenesis of the *Caenorhabditis elegans* dorsal hypodermis. *Dev Biol.* 1998;204(1):263-276. doi:10.1006/dbio.1998.9048
- Williams-Masson EM, Malik AN, Hardin J. An actin-mediated two-step mechanism is required for ventral enclosure of the C. elegans hypodermis. *Development*. 1997;124(15):2889-2901. doi:10.1242/dev.124.15.2889
- 12. Priess JR, Hirsh DI. *Caenorhabditis elegans* morphogenesis: The role of the cytoskeleton in elongation of the embryo. *Dev Biol.* 1986;117(1):156-173. doi:10.1016/0012-1606(86)90358-1
- 13. Costa M, Raich W, Agbunag C, Leung B, Hardin J, Priess JR. A putative catenin-cadherin system mediates morphogenesis of the *Caenorhabditis elegans* embryo. *J Cell Biol.* 1998;141(1):297-308. doi:10.1083/jcb.141.1.297
- Fukata Y, Itoh TJ, Kimura T, et al. CRMP-2 binds to tubulin heterodimers to promote microtubule assembly. *Nat Cell Biol*. 2002;4(8):583-591. doi:10.1038/ncb825
- Lin PC, Chan PM, Hall C, Manser E. Collapsin response mediator proteins (CRMPs) are a new class of microtubule-associated protein (MAP) that selectively interacts with assembled microtubules via a taxol-sensitive binding interaction. *J Biol Chem.* 2011;286(48):41466-41478. doi:10.1074/jbc.M111.283580
- 16. Wang LH, Strittmatter SM. Brain CRMP forms heterotetramers similar to liver dihydropyrimidinase. *J Neurochem*. 1997;69(6): 2261-2269. doi:10.1046/j.1471-4159.1997.69062261.x
- Tsuboi D, Hikita T, Qadota H, Amano M, Kaibuchi K. Regulatory machinery of UNC-33 Ce-CRMP localization in neurites during neuronal development in *Caenorhabditis elegans*.
   J Neurochem. 2005;95(6):1629-1641. doi:10.1111/j.1471-4159. 2005.03490.x
- 18. Ponnusamy R, Lebedev AA, Pahlow S, Lohkamp B. Crystal structure of human CRMP-4: correction of intensities for lattice-translocation disorder. *Acta Crystallogr D Biol Crystallogr*. 2014; 70(Pt 6):1680-1694. doi:10.1107/S1399004714006634
- 19. Hedgecock EM, Culotti JG, Thomson JN, Perkins LA. Axonal guidance mutants of *Caenorhabditis elegans* identified by filling sensory neurons with fluorescein dyes. *Dev Biol.* 1985;111(1): 158-170. doi:10.1016/0012-1606(85)90443-9
- Li W, Herman RK, Shaw JE. Analysis of the *Caenorhabditis elegans* axonal guidance and outgrowth gene unc-33. *Genetics*. 1992;132(3):675-689. doi:10.1093/genetics/132.3.675
- 21. Alexander M, Chan KKM, Byrne AB, et al. An UNC-40 pathway directs postsynaptic membrane extension in *Caenorhabditis elegans. Development.* 2009;136(6):911-922. doi: 10.1242/dev.030759
- 22. Kusch M, Edgar RS. Genetic studies of unusual loci that affect body shape of the nematode *Caenorhabditis elegans* and may code for cuticle structural proteins. *Genetics*. 1986;113(3):621-639. doi:10.1093/genetics/113.3.621
- 23. Praitis V, Ciccone E, Austin J. SMA-1 spectrin has essential roles in epithelial cell sheet morphogenesis in C. elegans. *Dev Biol.* 2005;283(1):157-170. doi:10.1016/j.ydbio.2005.04.002
- 24. Piekny AJ, Wissmann A, Mains PE. Embryonic morphogenesis in Caenorhabditis elegans integrates the activity of LET-502 Rho-binding kinase, MEL-11 myosin phosphatase, DAF-2 insulin receptor and FEM-2 PP2c phosphatase. *Genetics*. 2000; 156(4):1671-1689. doi:10.1093/genetics/156.4.1671
- 25. Ferguson EL, Horvitz HR. Identification and characterization of 22 genes that affect the vulval cell lineages of the nematode

- *Caenorhabditis elegans. Genetics.* 1985;110(1):17-72. doi:10. 1093/genetics/110.1.17
- Madeira F, Park YM, Lee J, et al. The EMBL-EBI search and sequence analysis tools APIs in 2019. *Nucleic Acids Res.* 2019; 47(W1):W636-W641. doi:10.1093/nar/gkz268
- Waterhouse AM, Procter JB, Martin DMA, Clamp M, Barton GJ. Jalview version 2—a multiple sequence alignment editor and analysis workbench. *Bioinformatics*. 2009;25(9): 1189-1191. doi:10.1093/bioinformatics/btp033
- 28. Garzanelli J, Maiden S. Exposing a Novel Genetic Interaction Between unc-33/CRMP and hmp-2/β-catenin During Caenorhabditis elegans Embryogenesis. microPublication Biology; 2020. doi:10.17912/MICROPUB.BIOLOGY.000286
- Chen J, Wang X, Zhu T, Zhang Q, Zhang JZH. A comparative insight into amprenavir resistance of mutations V32I, G48V, I50V, I54V, and I84V in HIV-1 protease based on thermodynamic integration and MM-PBSA methods. *J Chem Inf Model*. 2015;55(9):1903-1913. doi:10.1021/acs.jcim.5b00173
- Fu T, Zheng G, Tu G, et al. Exploring the binding mechanism of metabotropic glutamate receptor 5 negative allosteric modulators in clinical trials by molecular dynamics simulations. ACS Chem Nerosci. 2018;9(6):1492-1502. doi:10.1021/acschemneuro.8b00059
- 31. Shuaib S, Saini RK, Goyal D, Goyal B. Impact of K16A and K28A mutation on the structure and dynamics of amyloid- $\beta_{42}$  peptide in Alzheimer's disease: key insights from molecular dynamics simulations. *J Biomol Struct Dyn.* 2020;38(3):708-721. doi:10.1080/07391102.2019.1586587
- 32. Brenner S. The genetics of *Caenorhabditis elegans*. *Genetics*. 1974;77(1):71-94.
- Waterhouse A, Bertoni M, Bienert S, et al. SWISS-MODEL: homology modelling of protein structures and complexes. *Nucleic Acids Res.* 2018;46(W1):W296-W303. doi:10.1093/nar/gky427
- Lee RYN, Howe KL, Harris TW, et al. WormBase 2017: molting into a new stage. *Nucleic Acids Res.* 2018;46(D1):D869-D874. doi:10.1093/nar/gkx998
- 35. Mark P, Nilsson L. Structure and dynamics of the TIP3P, SPC, and SPC/E water models at 298 K. *J Phys Chem A*. 2001; 105(43):9954-9960. doi:10.1021/jp003020w

- Jorgensen WL, Madura JD. Quantum and statistical mechanical studies of liquids. 25. Solvation and conformation of methanol in water. *J Am Chem Soc.* 1983;105(6):1407-1413. doi:10.1021/ja00344a001
- 37. Maier JA, Martinez C, Kasavajhala K, Wickstrom L, Hauser KE, Simmerling C. ff14SB: improving the accuracy of protein side chain and backbone parameters from ff99SB. *J Chem Theory Comput.* 2015;11(8):3696-3713. doi:10.1021/acs.jctc.5b00255
- 38. Götz AW, Williamson MJ, Xu D, Poole D, Le Grand S, Walker RC. Routine microsecond molecular dynamics simulations with AMBER on GPUs. 1. Generalized born. *J Chem Theory Comput.* 2012;8(5):1542-1555. doi:10.1021/ct200909j
- Case, DA, Betz, RM, Cerutti, DS, et al. AMBER 2016. Published online 2016.
- Roe DR, Cheatham TE. PTRAJ and CPPTRAJ: software for processing and analysis of molecular dynamics trajectory data. *J Chem Theory Comput.* 2013;9(7):3084-3095. doi:10.1021/ ct400341p
- Humphrey W, Dalke A, Schulten K. VMD: visual molecular dynamics. *J Mol Graph*. 1996;14(1):33-38, 27–28. doi:10.1016/ 0263-7855(96)00018-5
- 42. Pettersen EF, Goddard TD, Huang CC, et al. UCSF chimera—a visualization system for exploratory research and analysis. *J Comput Chem.* 2004;25(13):1605-1612. doi:10.1002/jcc.20084
- Miller BR, McGee TD, Swails JM, Homeyer N, Gohlke H, Roitberg AE. MMPBSA.py: an efficient program for end-state free energy calculations. J Chem Theory Comput. 2012;8(9): 3314-3321. doi:10.1021/ct300418h

**How to cite this article:** Prins R, Windsor P, Miller BR III, Maiden S. Alleles of *unc-33*/CRMP exhibit defects during *Caenorhabditis elegans* epidermal morphogenesis. *Developmental Dynamics*. 2022;1-13. doi:10.1002/dvdy.497